

Contents lists available at ScienceDirect

Journal of Computational Physics

journal homepage: www.elsevier.com/locate/jcp



A three-dimensional numerical scheme for modeling discontinuous pinning at sharp edges using the Volume-of-Fluid method



Ashish Pathak¹, Wen Jin¹, Mehdi Raessi*

Department of Mechanical Engineering, University of Massachusetts Dartmouth, Dartmouth, MA 02747, USA

ARTICLE INFO

Article history: Received 12 July 2022 Received in revised form 24 December 2022 Accepted 30 January 2023 Available online 10 February 2023

Keywords:
Contact line
Pinning
Discontinuous pinning
Volume-of-Fluid
Multi-phase flow

ABSTRACT

We present a novel three-dimensional (3D) numerical scheme for modeling the discontinuous contact line pinning along sharp straight edges. The proposed scheme is devised for multi-phase flow solvers that rely on the Volume-of-Fluid (VOF) method, although its fundamental concepts can be extended and applied to other methods. Following the Piecewise-Linear-Interface-Construction (PLIC) approach in VOF, the discontinuous pinning is modeled by adjusting the orientation of PLIC polygons located near a sharp edge according to the pinning stage. That is achieved by solving a root-finding problem and using a 3D geometrical toolbox, where the advancing contact angle determines critical volume fractions in numerical cells neighboring the sharp edge. Implementing the proposed scheme in our multi-phase flow solver, we assessed its performance using several test cases where contact line pinning effects dominate. To demonstrate the scheme's efficacy, we present quantitative comparisons of our results at various grid resolutions and with a theoretical study. Furthermore, we show quantitatively that without a numerical treatment of contact line pinning, the simulation results will be drastically different. Contact line pinning plays a critical role in several technologies including separation, lithography, lens fabrication, micro-fluidic flow control among numerous others. The proposed scheme will help to accurately capture the pinning effects in computational simulations of such applications.

© 2023 Elsevier Inc. All rights reserved.

1. Introduction

When a liquid drop is deposited on a partially wetting surface, the wetted area on the substrate can be clearly identified. The curved line enclosing this wetted area, where all three phases, solid, liquid and the ambient gas, meet is called the contact line. Pinning of contact line occurs when the motion of the contact line is arrested by a physical or a chemical inhomogeneous feature. Physical features may include sharp edges (corners) in the path of contact line motion. Chemical inhomogeneity causes a jump in contact angle across the transition between hydrophilic and hydrophobic regions. The contact line is pinned along the transition and moves only when the contact angle overcomes the requisite jump. The contact line pinning may be categorized into continuous and discontinuous pinning [23]. In continuous pinning the entire

E-mail addresses: apathak@iitj.ac.in (A. Pathak), wjin@umassd.edu (W. Jin), mraessi@umassd.edu (M. Raessi).

^{*} Corresponding author.

¹ AP and WI have equally contributed to this work.

contact line is pinned. The contact line is only partially pinned in discontinuous pinning. The present work focuses on discontinuous pinning of contact line at edges (corners) and proposes a numerical scheme to model it.

During contact line pinning, the curvature of the liquid-gas interface changes, which in turn modifies the capillary forces. The contact line pinning is, therefore, stronger at smaller length scales. There are many applications in which the contact line pinning is exploited. Some examples include the drop-weight method [20,42] for determining surface tension; liquid-liquid extraction (LLE) microsystems [3] for extracting and concentrating target molecules; slot coating [13,29,37]; step and flash imprint lithography [36]; flow control in microchannels [19,27]; mass production of microlenses [25] and superhydrophobic surfaces [8,24,26,47]

Most studies on contact line pinning/depinning are thermodynamic analyses which predict stable and metastable states corresponding to global and local minima in the free energy profile [14,22,43]. A droplet remains in the metastable state unless external energy is provided, upon accepting which the droplet overcomes the energy barrier and attains a lower energy state [4,22]. The thermodynamic studies, however, do not predict the actual dynamic event of transition from one state to another. The transient transition includes the pinning/depinning event and can be captured by solving the hydrodynamic momentum equation governing the interfacial flow. Capturing such events can be critical for important applications such as lithography and liquid flow in microcavities studied by Reddy and Bonnecaze [36] and Goldschmidtboeing et al. [19], respectively.

Ferdowsi and Bussmann [16] and Ferdowsi [15] in their pioneering work, proposed a numerical scheme to model contact line pinning. However, their scheme was applicable to axisymmetric geometries, which implies continuous pinning. To the best of our knowledge, there is no flow solver currently available that models discontinuous pinning at straight sharp edges formed by two intersecting surfaces of different inclinations, where the contact line may wet both intersecting surfaces depending on the pinning strength. A novel numerical scheme is proposed for modeling discontinuous pinning in the context of the Volume-of-Fluid method, and its implementation into a multi-phase flow solver is also presented. The proposed algorithm is developed for mesh conforming solid geometries where the solid surfaces coincide with the faces of the computational cells. In this work, uniform Cartesian mesh is used, thus the sharp solid edges are formed by solid surfaces intersecting at 90°. Note that the focus of this work is not on contact angle hysteresis, where the contact angle varies due to changes in the velocity of a contact line moving on a flat surface. Modeling such contact angle hysteresis has been extensively discussed in the literature, for example, [11,12,39–41,45,46]. Contact angle hysteresis, as defined above, was not considered in this work on purpose to isolate discontinuous pinning effects, which only arise when the contact line meets and crosses a sharp edge.

The structure of the paper is as follows. In section 2, we present the equations governing the two-fluid flow, where the two fluids are separated by a sharp interface. Section 3 presents the numerical approach to solving the governing equations, along with the novel scheme to model the discontinuous pinning of the contact line. The performance of the proposed scheme is assessed by solving several test problems in section 4. Finally, section 5 presents concluding remarks.

2. Governing equations

Consider two immiscible fluids, fluid 1 and 2, separated by an interface. The fluids are assumed to be Newtonian and incompressible. The continuity and momentum equations are:

$$\nabla \cdot \mathbf{U} = 0 \tag{1}$$

$$\frac{\partial}{\partial t} (\rho \mathbf{U}) + \nabla \cdot (\rho \mathbf{U} \mathbf{U}) = -\nabla p + \nabla \cdot \tau + \mathbf{F}_B + \mathbf{F}_{ST}$$
(2)

Here, \mathbf{U} , ρ , and p are velocity vector, density and pressure, respectively. \mathbf{F}_B is the body force, e.g., gravity, \mathbf{F}_{ST} is the surface tension force and τ is the stress tensor, defined by:

$$\tau = \mu \left(\nabla \mathbf{U} + \nabla \mathbf{U}^T \right) \tag{3}$$

where μ is the dynamic viscosity coefficient. Following the Volume-of-Fluid method, to track the interface between the two fluids, we define a scalar f as:

$$f(\mathbf{x}) = \begin{cases} 1 & \text{if } \mathbf{x} \in \text{fluid 1} \\ 0 & \text{if } \mathbf{x} \notin \text{fluid 1} \end{cases}$$
 (4)

In a discretized computational domain, the volume fraction F is defined as the fraction of a cell volume, denoted by V, that is occupied by fluid 1, i.e.,

$$F = \frac{1}{V} \int_{V} f \, dv \tag{5}$$

which means the volume fraction of fluid 2 is 1 - F. In other words, fluid 2 need not be tracked explicitly. The tracking of the two fluids is done by solving the following transport equation:

$$\frac{\partial f}{\partial t} + (\mathbf{U} \cdot \nabla) f = 0 \tag{6}$$

The density appearing in the discretized form of eq. (2) is computed as:

$$\rho = F \,\rho_\ell + (1 - F) \,\rho_g \tag{7}$$

where, ρ_{ℓ} and ρ_{g} denote the densities of fluid 1 and fluid 2, respectively. The discretized coefficient of dynamic viscosity is computed from the following relation:

$$\frac{1}{\mu} = \frac{F}{\mu_\ell} + \frac{1 - F}{\mu_g} \tag{8}$$

where, μ_{ℓ} and μ_{g} are the coefficients of dynamic viscosity of fluid 1 and fluid 2, respectively. Harmonic averaging of μ ensures that fluid stresses do not result in excessive accelerations in less dense fluid near the interface [31,38].

No-slip and no-penetration boundary conditions are imposed at the wall boundaries of the computational domain:

$$\mathbf{U} \cdot \hat{\mathbf{n}} = 0 \tag{9}$$

$$\mathbf{U} \cdot \hat{\mathbf{t}} = 0 \tag{10}$$

Here, $\hat{\mathbf{n}}$ and $\hat{\mathbf{t}}$ are normal and tangent to the boundary walls, respectively. A zero pressure gradient is also imposed at the wall boundaries.

$$\frac{\partial p}{\partial n} = 0 \tag{11}$$

3. Numerical implementation

A detailed explanation of the solution procedure of eqs. (1), (2) and (6) can be found in [31]. A brief summary is provided in this section. Equation (2) is solved using the finite volume discretization on a staggered mesh following the marker and cell method [21]. In a staggered arrangement, velocity components u, v and w are located at cell faces in x-, y- and z-directions, respectively. All other field variables, such as f and p, are defined at cell centers. The two-step projection method of [10] was employed to solve eq. (2) in fractional steps:

$$\frac{\rho^{n+1}\mathbf{U}^* - \rho^n\mathbf{U}^n}{\Delta t} = -\nabla \cdot (\rho \mathbf{U} \mathbf{U})^n + \nabla \cdot (\tau)^n + \mathbf{F}_B$$
(12)

$$\frac{\rho^{n+1}\mathbf{U}^{n+1} - \rho^{n+1}\mathbf{U}^*}{\Delta t} = -\nabla p^{n+1} + \mathbf{F}_{ST}$$

$$\tag{13}$$

where superscripts n and n+1 denote previous and current times, respectively. U^* represents the intermediate velocity. The pressure Poisson equation is obtained by applying the continuity eq. (1) on eq. (13):

$$-\nabla \cdot \left(\frac{\nabla p^{n+1}}{\rho^{n+1}}\right) = -\frac{1}{\Delta t} \nabla \cdot \mathbf{U}^* - \nabla \cdot \left(\frac{\mathbf{F}_{ST}}{\rho^{n+1}}\right) \tag{14}$$

The pressure Poisson equation is solved using the multigrid preconditioned BiCGSTAB linear solver that was previously introduced in [33]. The multigrid preconditioned Poisson solver is fast because the number of iterations to converge does not increase with mesh resolution.

High density ratios are typical of multi-phase flow systems. To ensure numerical stability and to avoid artificial interface deformation in such flows, mass and momentum are consistently transported in a coupled manner [31]. Here the same volume fluxes are used to transport both mass and momentum, establishing a tight coupling between the two transports and avoiding unphysical numerical artifacts in simulations at high density ratios. The transport equation of scalar f, representing mass, is solved in a sharp manner using the geometric method of Youngs [44]. The interface is reconstructed following the Piecewise-Linear-Interface-Construction (PLIC) approach. In PLIC, a continuous interface is represented by a collection of discontinuous linear segments in 2D, an example of which is shown in Fig. 1, or by a series of planar polygons in 3D (see Fig. 17). The volume fraction F is also shown in Fig. 1(b). The volume fluxes at cell faces required in eq. (6) are calculated using the semi-analytical approach by Youngs [44], where two ingredients are required: interface orientation \hat{n}_f and the available discontinuous volume fraction F in a computational cell. Once the interface orientation and location in each cell are fixed, volume fluxes at the cell faces can be computed by calculating the area in 2D (volume in 3D) of each phase in the red rectangle (cuboid in 3D) shown in Fig. 2.

We will now briefly describe the scheme for computing the orientation of the PLIC interface. The normal vector to a PLIC interface is estimated using the relation:

$$\hat{n}_f = \nabla F / |\nabla F| \tag{15}$$

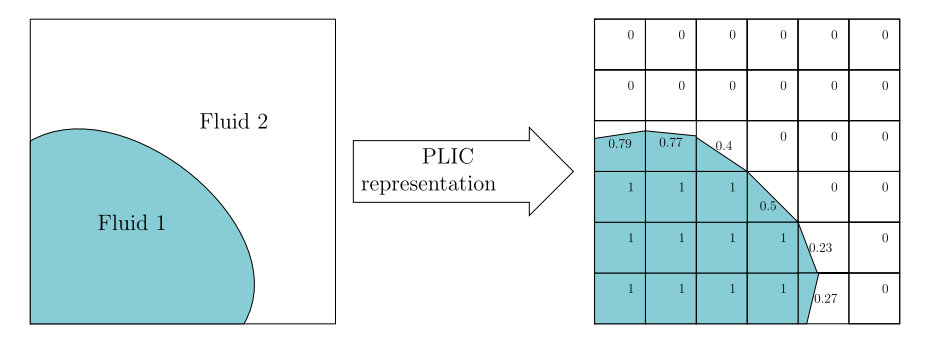


Fig. 1. (a) Schematic of an interface separating two immiscible fluids. (b) The PLIC approximation of the continuous interface shown in (a). The numbers on (b) show the discontinuous VOF field representing the volume fraction of fluid 1.

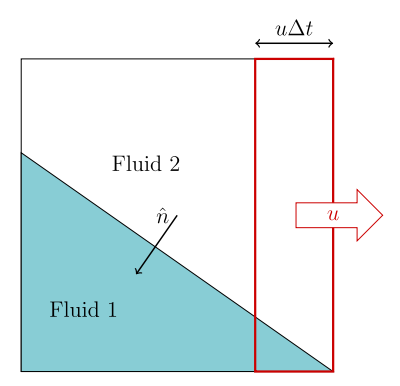


Fig. 2. Calculation of volume flux at the face of a donor finite volume cell. The volume flux of fluid 1 is represented by the colored area contained inside the red rectangle. In 3D, the red rectangle is a rectangular prism and the colored region inside the red rectangle is a trapezoidal prism. (For interpretation of the colors in the figure(s), the reader is referred to the web version of this article.)

A better approximation of \hat{n}_f can be obtained if the discontinuous F is replaced by a smoothened F. The discontinuous volume fraction F is smoothened in a radially symmetric manner using a widely used kernel proposed by Peskin [34]:

$$\delta_{\epsilon}^{\cos}(r) = \begin{cases} \left(1 + \cos\left(\frac{\pi r}{\epsilon}\right)\right)/c & r \le \epsilon \\ 0 & r > \epsilon \end{cases}$$
(16)

Here c normalizes the kernel and is defined as:

$$c = \int_{0}^{\epsilon} \left(1 + \cos\left(\frac{\pi r}{\epsilon}\right) \right) 2\pi r dr = \epsilon^{2} \left(\pi^{2} - 4\right) / \pi \text{ in 2D}$$
(17)

$$c = \int_{0}^{\epsilon} \left(1 + \cos\left(\frac{\pi r}{\epsilon}\right) \right) 4\pi r^{2} dr = \frac{4}{3} \epsilon^{3} \left(\pi^{2} - 6\right) / \pi \text{ in 3D}$$

$$(18)$$

The parameter ϵ is chosen to ensure that convolutions are restricted to $3\times 3\times 3$ stencil. Parameter r denotes the distance from the center of the kernel. Normal vector \hat{n}_f at cell vertices is calculated from the smoothened F. The \hat{n}_f at cell vertices are then averaged to obtain the \hat{n}_f at the cell center as illustrated in Fig. 3. The cell-centered \hat{n}_f determines the orientation of the PLIC interface. The normal vector \hat{n}_f can also be used to compute curvature $\kappa = -\nabla \cdot \hat{n}_f$, which is needed in the surface tension force calculation.

When the liquid-gas interface is in contact with a solid surface, a known contact angle θ_a is used as a boundary condition. The boundary condition is imposed by specifying the vertex normal vectors at the solid surface as shown in Fig. 4. In 3D, vertices are identified on the solid surface in a narrow band around the contact line as shown in Fig. 5. Assuming the solid surface to be perpendicular to the z-axis, the x-y orientations of the normals at these identified vertices are simply borrowed from the normals one cell removed from the solid surface. The z-component of the normal vector is then defined to represent the contact angle θ_a . Vertices that are two cells removed from the solid surface have the quantity F available in the full $4 \times 4 \times 4$ stencil, which is sufficient for \hat{n}_f calculation. Cells that are one cell removed from the solid surface require F in a stencil that penetrates one cell deep into the solid surface. Ideally, we should extend the liquid-gas interface and the

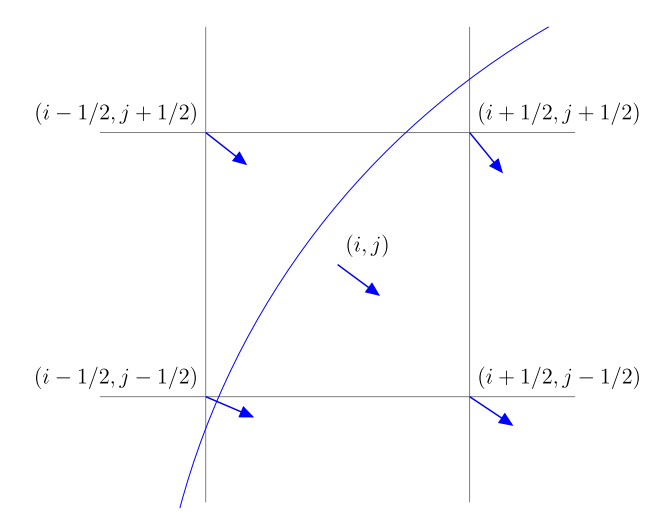


Fig. 3. Vertex-centered and cell-centered normals vectors in a 2D cell (i, j) containing the interface. In the present work, a 3D version is used.

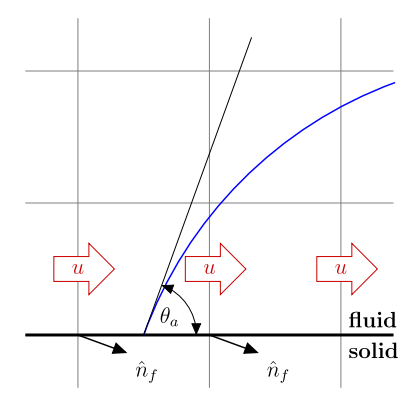


Fig. 4. Imposition of contact angle at the solid boundary. The unit normal vector \hat{n}_f of the phase interface at the solid boundary is modified to reflect the contact angle θ_a . While the no-slip boundary condition is applied on the solid, the face-centered horizontal velocities, u, which contribute to the VOF transport, including the cells containing the contact line, are half a cell above the solid surface, hence non-zero.

corresponding volume fraction field F into the solid surface. For practical purposes, just mirroring the values of $F_{i,j,k}$ from the fluid cells into adjacent solid cells was found sufficient [6,7].

The surface tension force is modeled with the balanced-force scheme proposed by [17]. The scheme builds upon the *Continuum Surface Force (CSF)* method of [5], and discretely establishes an exact balance between the pressure and surface tension as indicated in eq. (13). This, in turn, suppresses the spurious currents close to the interface.

Note that although the no-slip boundary condition is applied on the solid surface, the contact line is still able to slide on the surface because the advection of the VOF field, including the contact line, is carried out by face-centered velocities, shown in Fig. 4 (2D example). That is a common feature of the VOF method [1]. As seen in Fig. 4, in the numerical cell containing the contact line, the face-centered horizontal velocities are half a cell above the solid surface (hence non-zero). The VOF advection in contact line cells follows the same procedure of PLIC reconstruction and flux calculation that was discussed earlier.

3.1. Contact line pinning: interface reconstruction

Sharp edges on a substrate inhibit the motion of the contact line through the pinning phenomenon. The contact line momentarily comes to a halt due to the pinning effect, and can remain indefinitely pinned if sufficient energy is not supplied to the system to overcome the energy barrier associated with this metastable state. A common example of the contact line pinning can be found in the ability of a drinking glass with a sharp rim to hold slightly more water than its own volume.

A theoretical model of contact line pinning was first proposed by Gibbs [18]. We briefly describe Gibbs theory here. Consider a contact line approaching a sharp corner edge of angle ϕ as shown in Fig. 6 at the macro scale. It is only at the macro scale that the corner appears sharp; at the micro scale, however, the slope transition is rounded (not shown; see Ferdowsi [15, Fig. 6.1]). For simplicity, we assume that the advancing contact angle is constant and equal to θ_a . Before

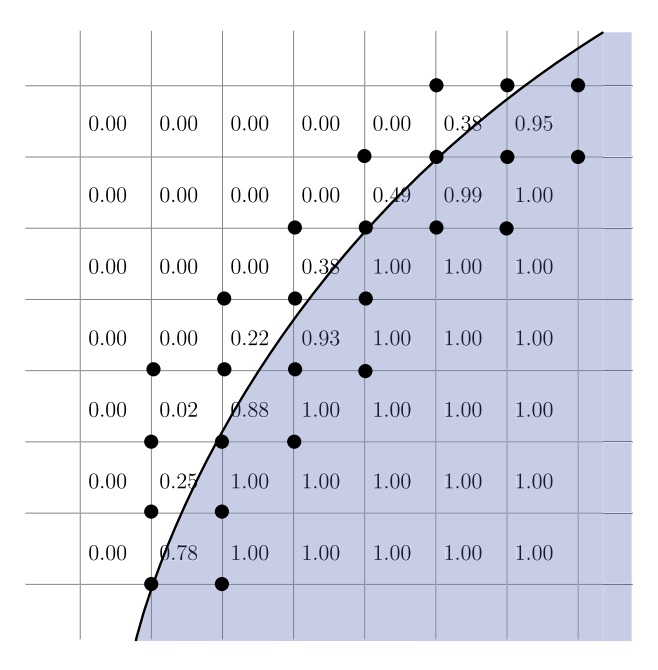


Fig. 5. A 3D contact line resting on a solid surface (top view looking down on the surface is shown). The numbers shown are volume fractions in cells adjacent to the solid surface. The vertices at which \hat{n}_f are modified to impose the contact angle are marked by bullets (\bullet).

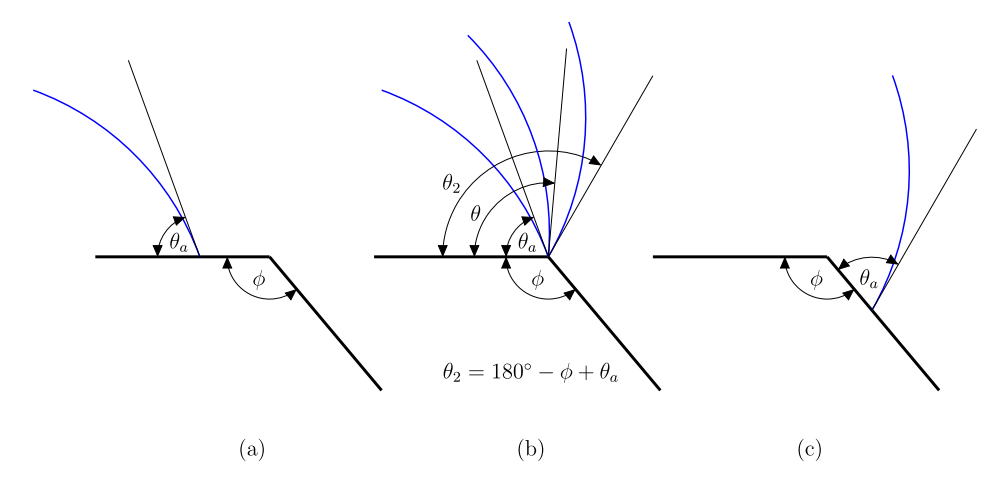


Fig. 6. A schematic showing orientation of the interface close to the contact line when (a) interface is approaching a sharp corner, (b) interface is at the sharp corner, (c) interface moves beyond the sharp corner.

reaching the sharp corner, this contact angle is maintained by the interface as demonstrated in Fig. 6(a). Upon reaching the sharp corner, the interface performs a rotation about this corner (Fig. 6(b)). During this rotation,

$$\theta_a \le \theta \le \theta_2 = (180^\circ - \phi + \theta_a) \tag{19}$$

The duration of rotation constitutes the interface pinning phenomenon. When θ becomes equal to $180^{\circ} - \phi + \theta_a$, the contact angle corresponds to the advancing contact angle of the inclined surface. Upon reaching this state, the contact line depins and the interface starts sliding down the inclined surface (Fig. 6(c)).

The theoretical model of Gibbs [18] mentioned above was validated experimentally by Oliver et al. [30], where droplets were bounded at the edge of a circular cylinder that had $\phi=90^\circ$. The phenomenon of pinning has been studied either experimentally or by using tools that compute energetically stable states. The only study that proposed a model that could predict dynamic rotation of interface during pinning was by Ferdowsi [15], Ferdowsi and Bussmann [16]. They proposed a numerical scheme to compute interface orientation and volume fluxes during continuous pinning in axisymmetric geometries.

The numerical scheme proposed in the present work is an extension of Ferdowsi [15] to discontinuous pinning in 3D non-axisymmetric problems. In discontinuous pinning, some points on the contact line may undergo pinning, while the rest

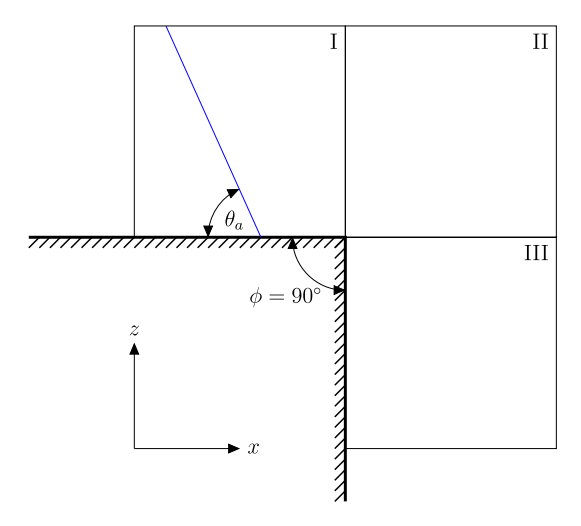


Fig. 7. The PLIC interface shown by the blue line in cell I makes an angle θ_a with the bottom surface. The interface also enters cells II and III when it pins and rotates at the corner.

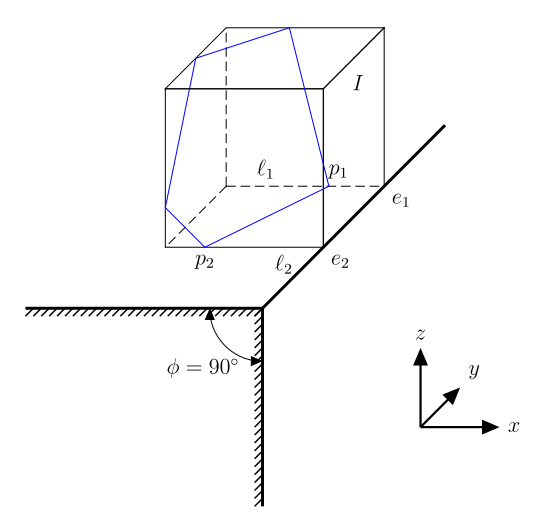


Fig. 8. PLIC interface in computational cell I. Lines ℓ_1 and ℓ_2 are coincident with the lower side edges of the cell. Points p_1 and p_2 are both behind the sharp corner edge.

do not; or all points on the contact line undergo pinning, but they are at different stages of rotation at any given time. The numerical scheme proposed by Ferdowsi [15] cannot be applied to such problems, and we are not aware of any numerical scheme that can model discontinuous pinning. To handle such problems, we propose a novel scheme, which is described below.

Consider a PLIC interface approaching a sharp corner of $\phi=90^\circ$ as shown in Fig. 7. The figure shows three cells neighboring the corner, which are labeled I to III. The PLIC interface approaches cell I from the left. Before entering cell I, the PLIC interface makes an advancing contact angle of θ_a with the substrate surface.

When the interface enters cell I, the following algorithm is used:

- 1. Compute the orientation of the PLIC interface using the VOF-based method proposed by Bussmann et al. [7]. Now that the orientation is known, the location of this interface is fixed by matching the volume fraction intercepted by the PLIC interface with the known volume fraction. This is accomplished by following the method of Youngs [44].
- 2. After both the location and orientation of the PLIC interface are computed, its intersection with the lower side edges of the computational cell can be identified. The lower side edges are labeled by lines ℓ_1 and ℓ_2 as shown in Fig. 8. The points of intersection of the PLIC interface with ℓ_1 and ℓ_2 are named p_1 and p_2 , respectively. The intersection of the lines ℓ_1 and ℓ_2 with the sharp corner edge results in points e_1 and e_2 , respectively. A critical volume fraction, $F^{\text{crit},1}$ is also computed by fixing p_1 at e_1 and p_2 at e_2 , and keeping the contact angle $\theta = \theta_a$. This is illustrated in Fig. 9. The 3D geometric toolbox of Pathak and Raessi [32] is used to compute the intercepted volume by this PLIC interface. Now,

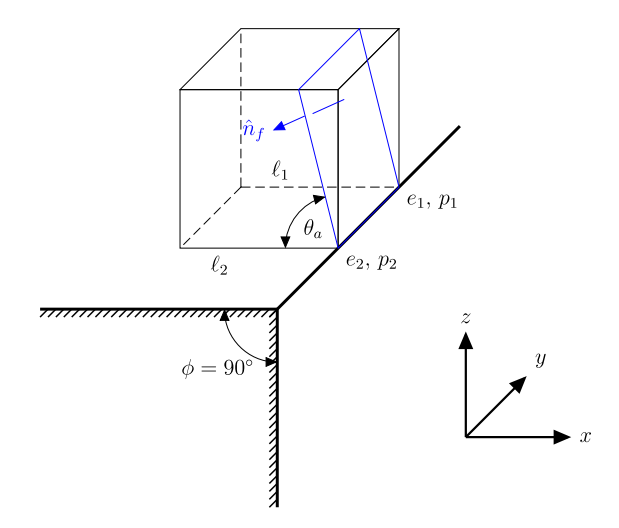


Fig. 9. The calculation of $F^{\text{crit},1}$, given a contact angle $\theta = \theta_a$.

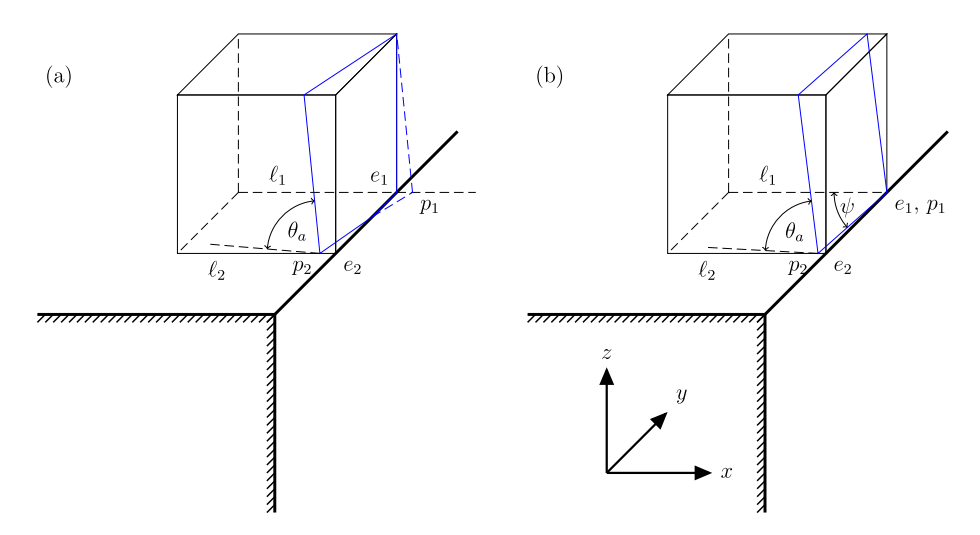


Fig. 10. (a) A PLIC interface without contact line pinning reconstructed from the method of Bussmann et al. [7], (b) The modified PLIC reconstruction based on the proposed pinning algorithm, where point p_1 coincides with e_1 .

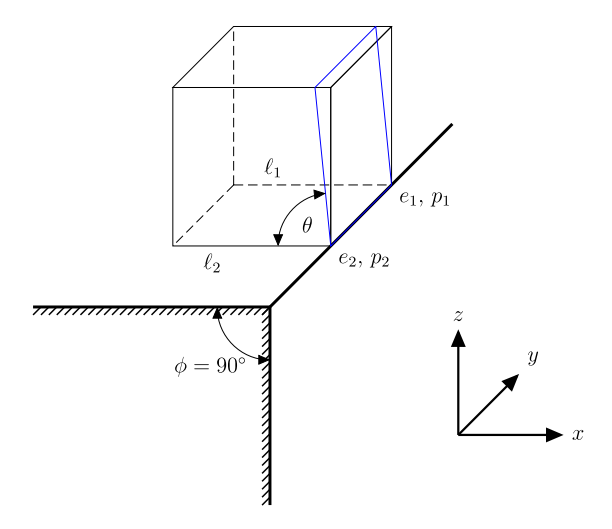


Fig. 11. PLIC reconstruction in the interfacial cell close to edge when $F^{known} > F^{crit,1}$.

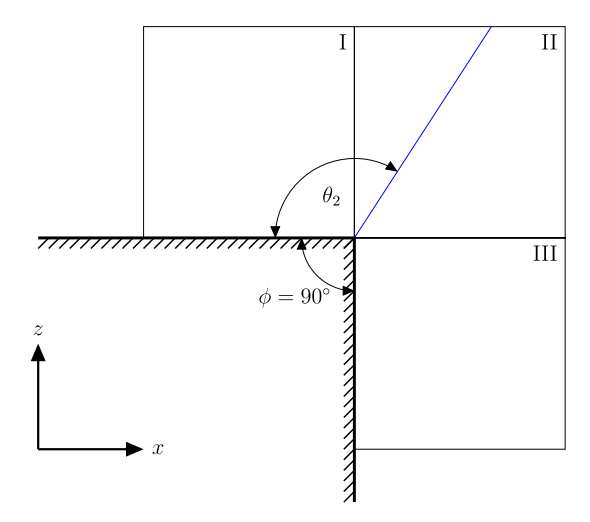


Fig. 12. Pinning rotation of the PLIC interface in cell II. Here, $\theta_2 = 180^{\circ} - \phi + \theta_a$ as defined in eq. (19).

denoting the volume fraction in cell I by F^{known} , the following three scenarios are possible based on the locations of p_1 and p_2 :

- (a) $F^{\text{known}} < F^{\text{crit},1}$ and both p_1 and p_2 are behind the sharp corner edge (see Fig. 8), i.e., the *x*-coordinates of both p_1 and p_2 are less than the *x*-coordinate of the sharp edge (in this example, where the edge is parallel to the *y*-axis).
- (b) $F^{\text{known}} < F^{\text{crit},1}$ and exactly one point between p_1 and p_2 is behind the sharp corner edge, and the other one is ahead of the sharp corner edge. An example is shown in Fig. 10(a).
- (c) $F^{\text{known}} > F^{\text{crit.,1}}$
- 3. When case (a) is encountered, we accept the PLIC orientation and location already computed in step 1.

If case (b) is encountered, we identify the point between p_1 and p_2 that is ahead of the sharp corner edge. Suppose point p_1 is ahead of the edge as shown in Fig. 10(a). In the illustration, point p_1 lies outside the cell and is the intersection between the prolonged PLIC interface and line ℓ_1 extended beyond the cell. Here, we do not accept the reconstruction performed in step 1. Instead, the interface is fixed at point e_1 , i.e., point p_1 coincides with e_1 . Keeping contact angle $\theta = \theta_a$, the PLIC interface is rotated about a vertical axis (in the z-direction in this example) passing through e_1 , until the volume intercepted by the PLIC interface matches the known volume fraction at some angle ψ . Here the angle ψ is the horizontal angle (in the x-y plane) between the contact line p_1p_2 and the line ℓ_1 as shown in Fig. 10(b). In other words, the following root-finding problem is solved:

$$F^p(\psi) - F^{\text{known}} = 0 \tag{20}$$

The calculation of the predicted volume fraction F^p requires the volume of a computational cell intercepted by the PLIC interface. This volume is computed using the 3D geometric toolbox developed by Pathak and Raessi [32]. Similar toolbox was developed by Baggio and Weigand [2]. To solve the root-finding problem given by eq. (20), Brent's method is used [35]. The computed ψ and the known θ define the orientation of the PLIC interface. The point p_1 fixed at e_1 specifies the location of the interface.

If the case (c) in step 2 is encountered, then the reconstruction in step 1 is not accepted. The PLIC interface is assumed to contain the edge line of the sharp corner as shown in Fig. 11. The PLIC interface is now free to rotate about an axis of rotation that is aligned with the sharp corner edge line. The PLIC interface is rotated until the predicted volume fraction equals the known volume fraction for some θ . In essence, we solve the following root-finding problem using the Brent's method:

$$F^{p}(\theta) - F^{\text{known}} = 0 \tag{21}$$

where $F^p(\theta)$ is the volume fraction of the computational cell intercepted by the PLIC interface subtending an angle θ with the substrate surface as shown in Fig. 11. The computed θ and the known $\psi = 90^\circ$ specify the orientation of the PLIC interface.

Due to the proposed approach presented above, as more liquid enters cell I from the left cell face, the interface will first appear to rotate about a vertical axis passing through either e_1 or e_2 . At the end of this horizontal rotation, the PLIC interface will eventually become aligned with the sharp corner edge. Once aligned, more liquid entry will result in the PLIC

Table 1 Properties of water and air, denoted by subscript ℓ and g, respectively.

| $ ho_\ell \; (\mathrm{kg}\mathrm{m}^{-3})$ | $\rho_{\rm g}~({\rm kgm^{-3}})$ | μ_ℓ (kg m $^{-1}$ s $^{-1}$) | $\mu_g \; ({\rm kg}{\rm m}^{-1}{\rm s}^{-1})$ | $\sigma (\mathrm{N} \mathrm{m}^{-1})$ |
|--|---------------------------------|--------------------------------------|---|---|
| 1000 | 1.226 | 1.137×10^{-3} | 1.78×10^{-5} | 7.286 ×10 ⁻² |

interface rotation about the sharp corner edge as the axis of rotation. This second rotation is called *pinning rotation* because the contact line becomes pinned at the sharp corner edge.

After cell I becomes full with liquid, the liquid is now allowed to flow into cell II. As a result, the PLIC interface now resides in cell II. At this point we compute a volume fraction $F^{\text{crit},2}$ corresponding to $\theta_2 = 180^{\circ} - \phi + \theta_a$ in Fig. 12. If the volume fraction in cell II $F^{\text{known}} < F^{\text{crit},2}$, the PLIC interface orientation is computed by assuming that the interface contains the sharp corner edge, and the PLIC interface is rotated about the edge until the corresponding volume fraction in cell II equals F^{known} . The same equation (21) is solved, only this time F^p and F^{known} correspond to those in cell II. When $F^{\text{known}} > F^{\text{crit},2}$, the PLIC interface is assumed to be depinned and its orientation satisfies the contact angle θ_a associated with the vertical surface. The PLIC interface, in this depinned state, is reconstructed using the method of Bussmann et al. [7] that was briefly explained earlier.

Due to the numerical scheme proposed above for cell II, the interface will be pinned at and rotate about the sharp corner edge as long as $\theta < 180^{\circ} - \phi + \theta_a$. When θ increases to $180^{\circ} - \phi + \theta_a$ due to this rotation, the interface orientation satisfies the contact angle θ_a associated with the vertical surface and it becomes depinned. After depinning, the interface is free to slide down the vertical surface. The proposed scheme is thus aligned with the theory of Gibbs [18].

The methodology proposed in the current work assumes that the computational mesh conforms with the solid geometry, i.e., the surfaces of the solid geometry coincide with the faces of computational cells. For simulations with Cartesian grids, this implies that only $\phi=90^\circ$ is possible at the corners. Therefore, only test cases corresponding to $\phi=90^\circ$ are considered here. For handling other values of ϕ , an unstructured grid may be required along with a suitable implementation of the VOF framework, e.g., in Lv et al. [28].

3.2. Contact line pinning: volume fluxes

During contact line pinning, fluid 2, i.e., gas, is allowed to cross the face shared by cells I and II before the liquid, e.g., water. In other words, gas is allowed to pass before liquid through the face shared by cells I and II when the PLIC interface is performing horizontal and vertical rotations. Similarly, when the interface is in cell II and rotating about the sharp corner, the gas is allowed to cross the face shared by cells II and III before the liquid. This approach is adopted from Ferdowsi [15].

The modified flux advection during pinning is further illustrated here with the help of Fig. 2. Suppose the cell shown here corresponds to cell I in Fig. 12. The liquid (fluid 1) and gas (fluid 2) volumes contained in the cell shown in Fig. 2 are FV_{cell} and $(1-F)V_{\text{cell}}$, respectively. The volume inside the red rectangle, V_{ε} , represents the volume advected out of the cell due to the face-centered velocity component u in a time step Δt . In the absence of pinning, e.g., in cells away from the edge, both liquid and gas phases contained inside the red rectangle would be advected out of the cell. In cell I, however, as long as the interface is undergoing pinning, no liquid is allowed to advect out before gas. The advection is done by implementing the following scheme. If sufficient gas volume is available in the cell, only gas is advected out in a particular time step. In other words, if $V_{\varepsilon} < (1-F)V_{\text{cell}}$, the advected gas volume is modified to V_{ε} and no liquid is advected out of the cell. If, however, gas volume available in the cell is less than V_{ε} , the gas in the cell is advected out first, followed by the liquid. Thus, if $V_{\varepsilon} \ge (1-F)V_{\text{cell}}$ the advected gas volume is modified to V_{ε} and the advected liquid volume is modified to $V_{\varepsilon} - (1-F)V_{\text{cell}}$.

4. Results

This section starts with a validation test case where the computed interface profile is compared to a theoretically known one. We then apply the proposed methodology to problems where the interface undergoes discontinuous pinning. The fluids in these problems are water and air, the properties of which are listed in Table 1. In addition, the dimensionless Weber number, $We = \rho_{\ell} V^2 D/\sigma$, and capillary number, $Ca = \mu_{\ell} V/\sigma$, are reported for each problem. Here, σ is the surface tension coefficient, V is the characteristic velocity and D is the characteristic length.

4.1. Contact line pinning in a spreading 2D Cartesian drop

This test case has been adopted from [16]. A sessile 2D Cartesian drop is resting on a pedestal with an initial contact angle of 75° as shown in Fig. 13. The associated geometric parameters are h=26.8 mm and r=103.5 mm. Using the symmetry of the problem, only half of the domain is simulated. At t=0, the contact angle is suddenly changed to $\theta=30^\circ$. The simulation is run for two pedestal sizes: l=7 Δx and l=8 Δx , where the computational cell size $\Delta x=15.625$ mm.

On a flat surface, the drop will spread freely until it attains an equilibrium profile corresponding to a contact angle of 30°. In the presence of a sharp edge, however, the contact line pins to the edge, which prevents the drop from spreading further. The simulation results are shown in Fig. 14 and compared to the theoretically known drop profile at equilibrium, shown in

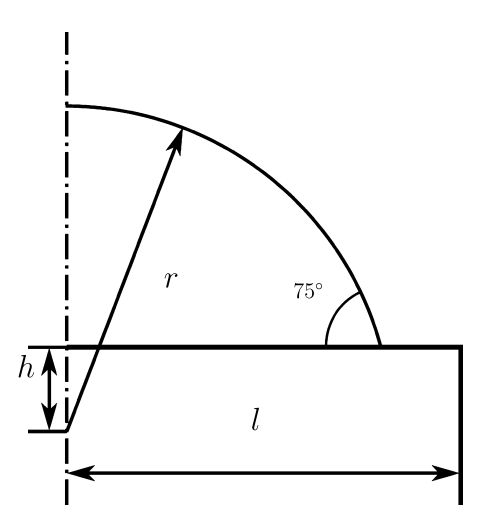


Fig. 13. Geometrical parameters of the test case in section 4.1.

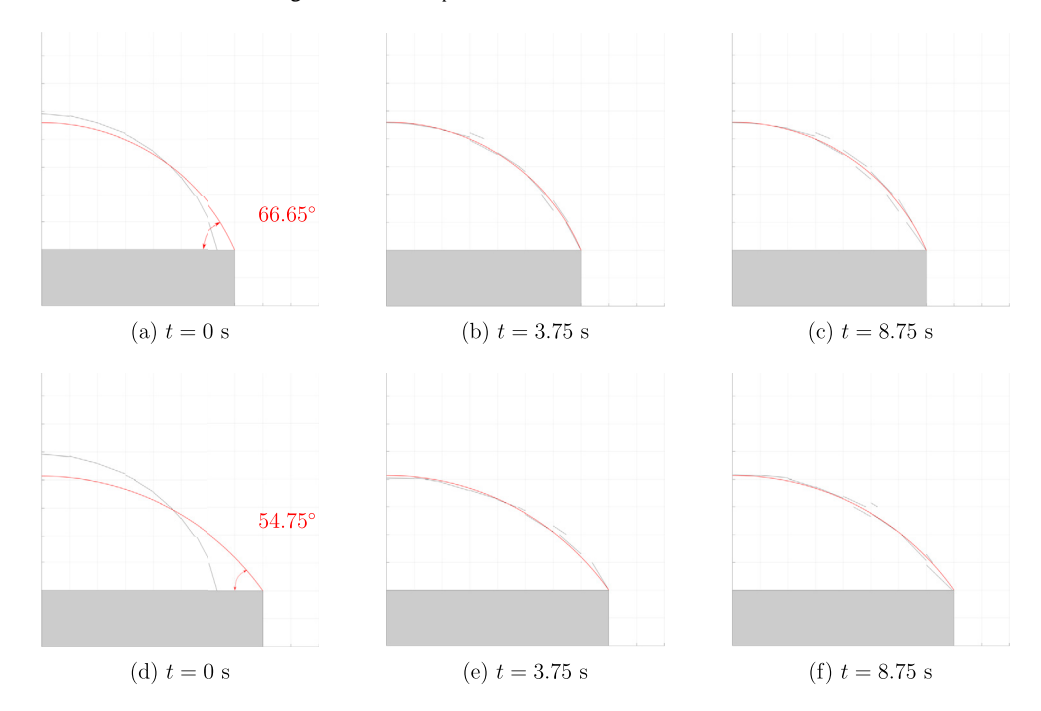


Fig. 14. Simulations results corresponding to pedestal length $l = 7\Delta x$ (first row) and $l = 8\Delta x$ (second row), where $\Delta x = 15.625$ mm. The exact theoretical profile is shown in red, and simulated PLIC interface is shown in black.

red, which is obtained using the pedestal size and drop volume (area). We find that the simulated profiles demonstrate a decent agreement with the theoretical profile; however, they appear to oscillate about the exact profile even after a long time (t = 8.75 s), which is consistent with the observations of Ferdowsi and Bussmann [16]. The oscillations are caused due to spurious currents induced by inaccuracies in curvature estimation [17].

4.2. Contact line pinning along straight edge

In this test case, a sessile water drop is made to slide down an inclined surface with an inclination angle of $\varphi=30^\circ$. The inclined surface ends abruptly in a sharp straight edge at an angle of $\phi=90^\circ$ as shown in Fig. 15. Radius of the sphere to which the cap belongs is $R_0=3.2$ mm. The contact angle is prescribed as $\theta_a=60^\circ$. The center of the sessile drop is initially located at a distance of 3.8 mm from the left face of the computational domain as shown in Fig. 15(b). The drop is given an initial uniform velocity of 0.25 m/s along the incline. Taking the characteristic length D to be $2R_0\sin(\theta_a)=5.54$ mm and characteristic velocity V to be 0.25 m/s, we obtain We=4.75 and Ca=0.0039. The gravity, g=9.8 m s⁻², is acting vertically downward. The size of the computational domain is 12.8 mm \times 19.2 mm \times 9.6 mm. The domain contains a solid

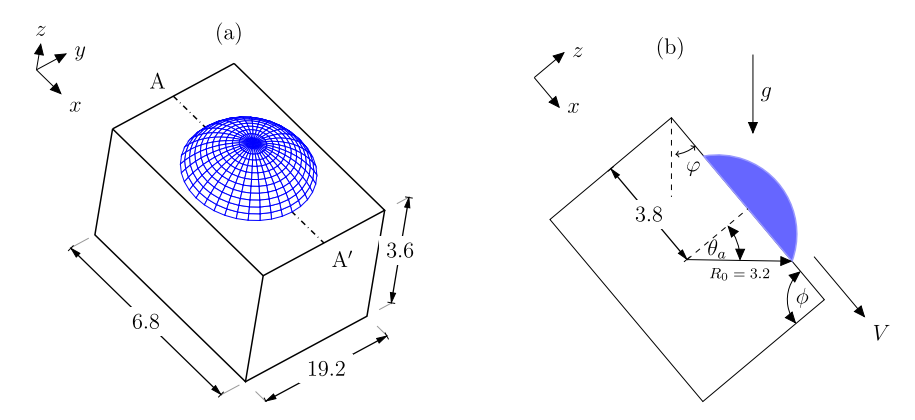


Fig. 15. (a) Isometric and (b) and side view of a liquid spherical cap of radius R_0 , representing a sessile water drop on an inclined surface with a sharp straight edge at an angle of $\phi = 90^\circ$. The contact angle $\theta_a = 60^\circ$, and inclination angle $\varphi = 30^\circ$. The drop is given an initial uniform velocity of V = 0.25 m/s along the incline. All units in mm. Drawings not to scale.

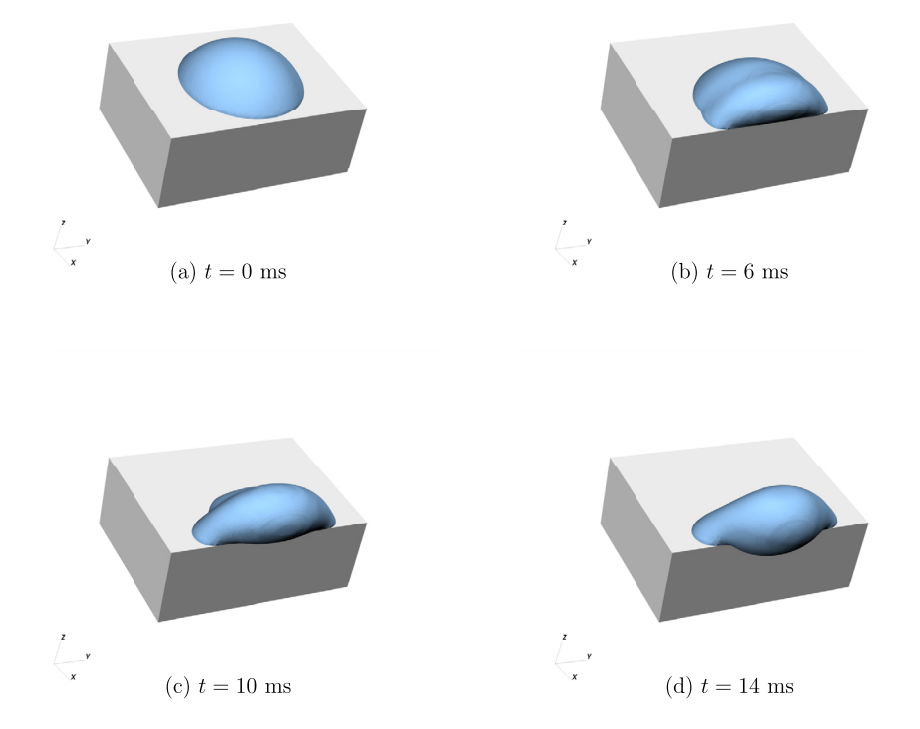


Fig. 16. Simulation results of discontinuous contact line pinning as a sessile water drop slides on an inclined surface with a sharp edge. We = 4.75 and Ca = 0.0039.

block of size 6.8 mm \times 19.2 mm \times 3.6 mm on which the sessile drop slides (see Fig. 15). Simulations were performed at four different mesh resolutions of 16, 32, 64 and 128 cells-per-diameter (CPD), where the diameter is $2R_0 = 6.4$ mm.

Fig. 16 shows the results of the 32 CPD simulation, depicting various instances in time as the sliding drop is pinned along the straight edge. Due to the circular geometry of the contact line, different portions of the contact line arrive at the straight edge at different times. The contact line hence demonstrates discontinuous pinning. As can be seen in Fig. 16, the downward sliding motion of the liquid is hindered at the edge due to pinning, forcing the liquid to spread laterally along the edge. Shortly after t = 6 ms, the pinned contact line in the middle of the liquid forms the appropriate contact angle with the vertical side of the solid block, parallel to the y - z plane, allowing the liquid to flow downward again. That eventually reduces the length of the wetted portion of the edge.

To provide a detailed view of the PLIC surfaces undergoing pinning treatment, the snapshot of the sliding drop at t = 5.2 ms, illustrated in Fig. 17(a), is used as an example. Fig. 17(b) depicts the PLIC surfaces representing the liquid-gas interface contained in the boxed region shown on Fig. 17(a). Focusing on the sharp edge, note the difference in the degrees of rotation of various PLIC surfaces, where those in the middle have performed the rotation motions the furthest. Also, note that the gap between the PLIC surfaces is expected as the PLIC approach does not require the reconstructed interfaces to be joined or continuous across neighboring cells.

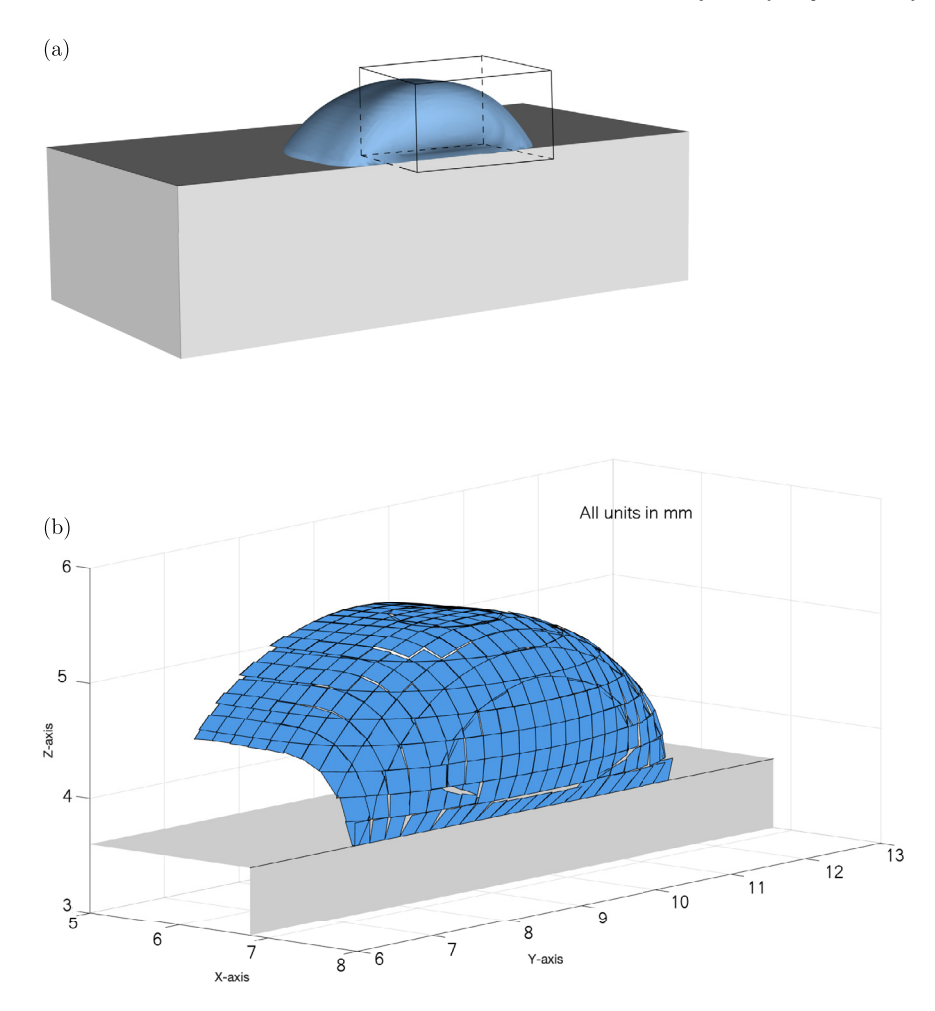


Fig. 17. (a) Snapshot of the water drop pinned along the sharp edge at t = 5.2 ms. The box shows the region for which the PLIC representation of the liquid-gas interface is provided in image (b) at the same time. Notice the various degrees of rotation of the PLIC segments at the contact line pinned at the sharp edge.

Next, we present the grid convergence study in Fig. 18, focusing on two quantities: width w, which is the portion of the straight edge wetted by the liquid (see Fig. 18(a)), and depth d, which is the distance in the negative z-direction from the straight edge to the extremum point which is wetted by the liquid. Fig. 18(b) and (c) show the time histories of d and w, respectively, obtained at four different mesh resolutions. Fig. 18(b) shows that around t = 7.0 ms the liquid starts to spread to the vertical face of the sharp edge, parallel to the y - z plane, resulting in mass redistribution, which eventually affects w. As Fig. 18(c) illustrates, w first rapidly increases as the leading of the drop meets and becomes pinned at the edge, while the rest of the contact line is catching up. However, as the liquid starts to move down again, the slope of w continues to decrease, and at approximately t = 11 ms, w starts to decrease with time. Results at various mesh resolutions show that the 16 CPD resolution is not sufficient to accurately capture the pinning. The results at mesh resolution of 32 CPD and above are very close, with 64 and 128 CPD results being the closest.

To demonstrate the efficacy and importance of the proposed scheme, we repeated the 32 CPD simulation without any numerical treatment for contact line pinning (i.e., the proposed scheme was turned off). Fig. 19 presents a quantitative comparison with respect to d and w between the two simulations: with and without the numerical treatment of contact line pinning. A drastic difference is seen in both d and w between the two cases. Without any pinning treatment, d starts increasing as soon as the leading front of the contact line reaches the sharp edge at about t = 0.92 ms. That is evident in the inlay of Fig. 19(a) and indicates that in the absence of pinning effects to resist or arrest the contact line motion, the drop "spills" over the sharp edge easily. As expected, in the simulation with the proposed pinning treatment, the contact line is pinned much longer, and it is not until t = 7.5 ms that the drop flows over the sharp edge. Similarly, without any pinning treatment, the sharp edge wetting occurs at a larger extent and earlier in time, as seen in Fig. 19(b).

In Fig. 20, we show a comparison of the top view between the simulations with (left column) and without (right column) the pinning treatment to illustrate why the wet width w is larger without the pinning treatment. In general, if a circle passes over a straight edge, the wetted width w increases in time until w becomes equal to the diameter of the circle.

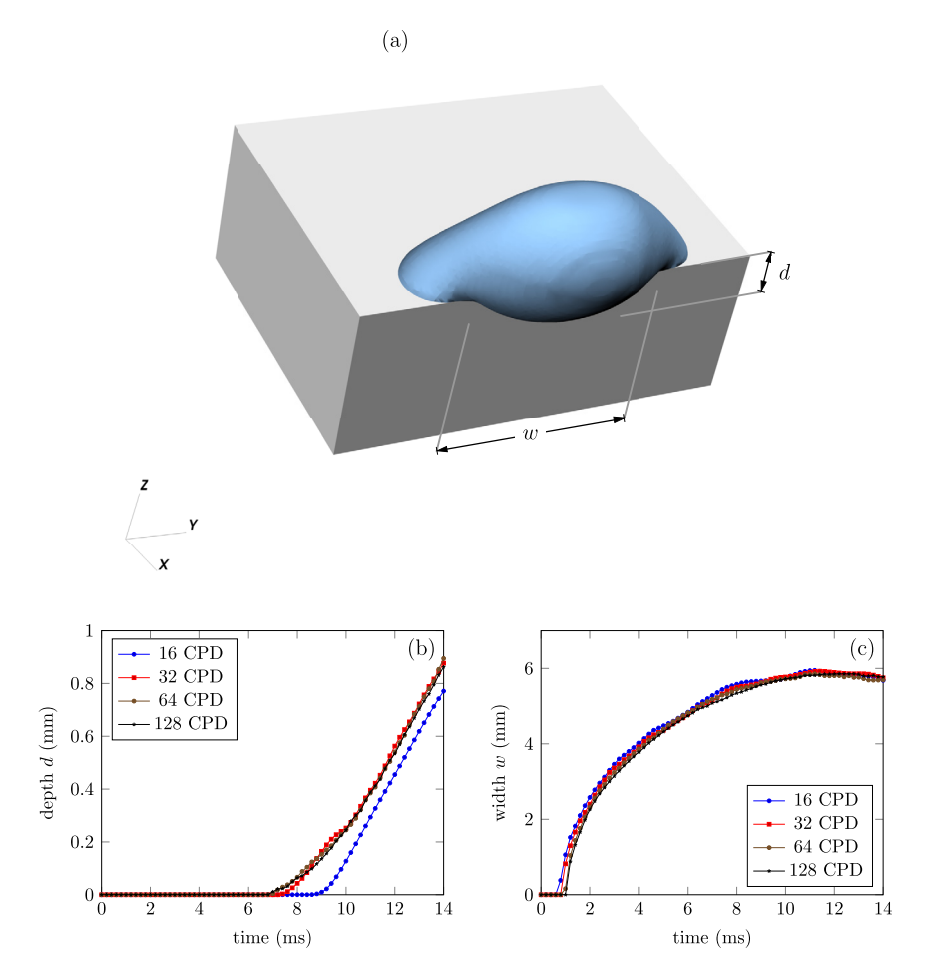


Fig. 18. (a) Wetting depth *d* and width *w* in discontinuous pinning of a sessile drop sliding on a surface with a sharp edge. Time histories of (b) *d* and (c) *w* obtained at various mesh resolutions, reported as the number of cells-per-diameter (CPD).

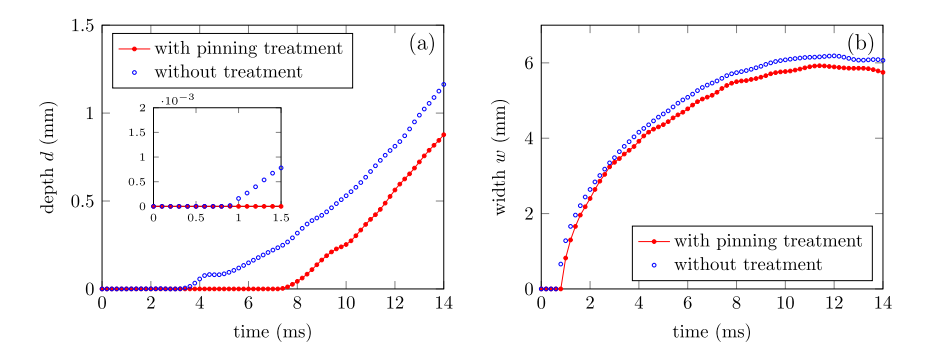


Fig. 19. Quantitative comparisons of (a) wetting depth d and (b) width w between two simulations of the sliding sessile drop, with and without the proposed numerical treatment of contact line pinning. Both simulations are at 32 CPD resolution.

The increase in w would be purely due the circular shape. Without the pinning treatment, the circular contact line passes over the straight edge in a somewhat uninhibited manner compared to when pinning treatment is used. Due to the pinning treatment, the motion of the contact line is momentarily arrested at the straight edge, which in turn, slows down the portions of the contact line in the transverse direction approaching the sharp edge - see the contact line encircled in red in Fig. 20 at t = 6 ms. That ultimately leads to a smaller w in the case with the pinning treatment at any given time. The impact of the pinning treatment on the drop geometry as a whole can also be seen in snapshots shown in Fig. 20. The contact line profiles with and without the pinning treatment differ; for example see the images for t = 14 ms.

To ensure that the proposed pinning treatment is not affecting the discrete mass conservation of the VOF method, we compared the total liquid volume as a function of time between the above two cases at 32 CPD with and without the

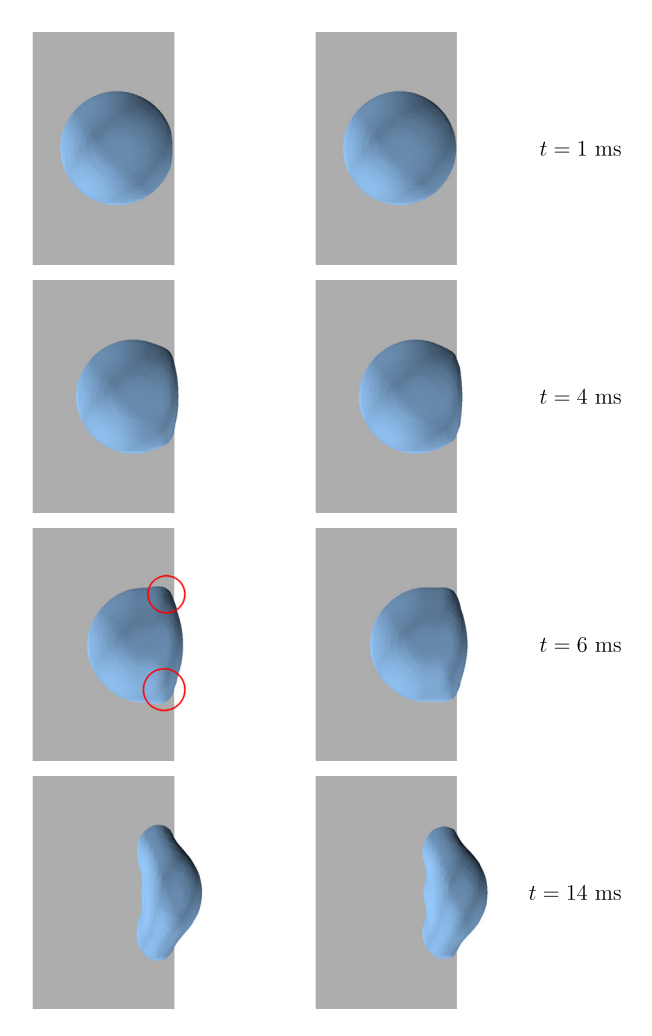


Fig. 20. Top view comparison between two simulations of the sliding sessile drop with (left column) and without (right column) the proposed pinning treatment at 32 CPD resolutions.

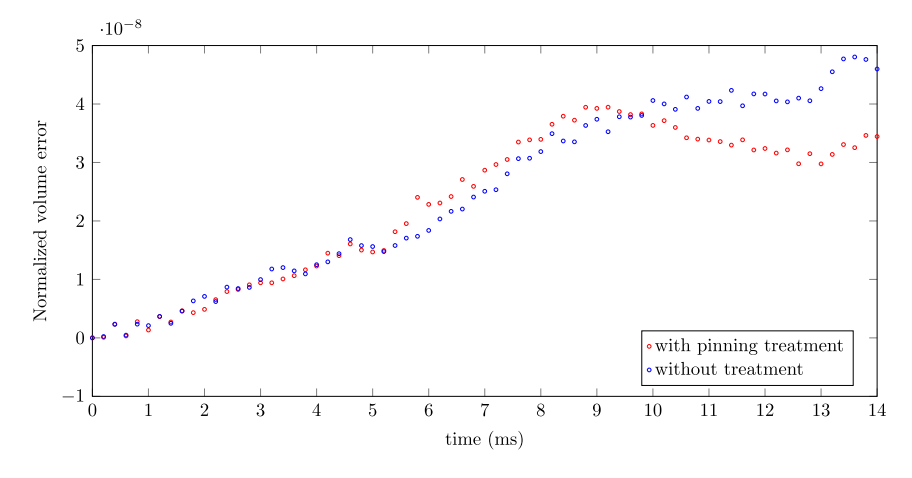


Fig. 21. Time history of normalized volume error in two simulations of the sliding sessile drop, with and without the proposed pinning treatment performed at 32 CPD resolution. The normalized volume error is defined as $(V_0 - V_t)/V_0$, where V_t and V_0 denote the liquid volumes at time t and t = 0, respectively.

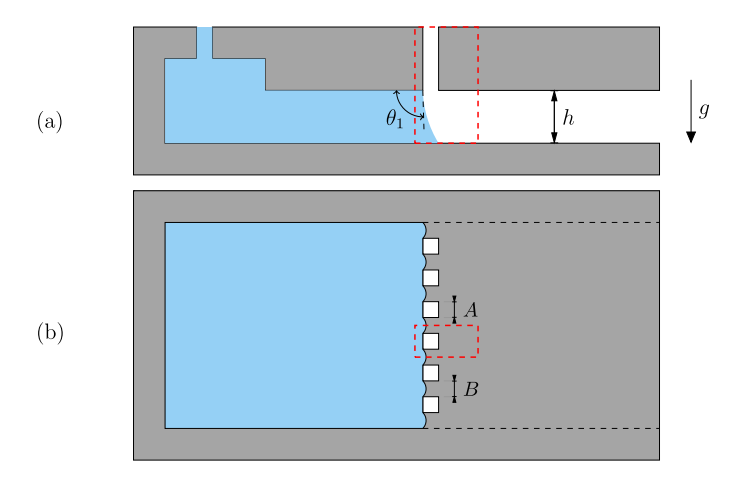


Fig. 22. (a) Side view and (b) top view of the parallel gap module where water (blue) makes a contact angle θ_1 at the hole edge. The computational domain is shown in the dashed red rectangle.

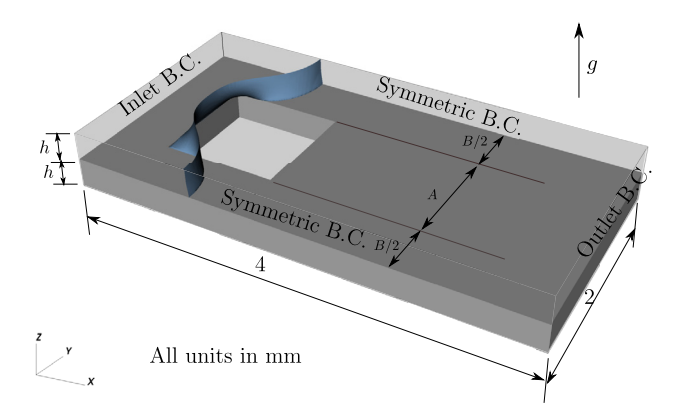


Fig. 23. Computational domain used for discontinuous pinning around a row of holes in a parallel gap. The transparent region along with the hole represents the portion open to the flow. The opaque gray region is closed to the flow and its boundaries act as walls. The water-air interface is shown in blue. Here, A = B = 1 mm and h = 0.25 mm.

pinning treatment. A normalized volume error is defined as $(V_0 - V_t)/V_0$, where V_t and V_0 denote the liquid volumes at any time t and t = 0, respectively. Fig. 21 shows the time history of the normalized volume error with and without the pinning treatment. As seen the normalized error remains below $\sim 5 \times 10^{-8}$ (or 5×10^{-6} %) in both cases, confirming that the proposed treatment does not negatively impact the discrete mass conservation of the VOF method.

4.3. Discontinuous pinning around a row of holes in a parallel gap

This test case has been adopted from Hu et al. [23], who studied the discontinuous pinning around the holes of an immersion hood, also called shower head, employed for water extraction in lithography. The schematic of the parallel gap module is shown in Fig. 22.

The upper plate of the parallel module has a row of evenly spaced holes. As the air-water interface moves in the parallel gap of height h, the contact line becomes pinned at the edges of the holes. The edge length of the square holes is A and the gap between consecutive holes is B as illustrated in Fig. 22(b). For this study, A = B = 1 mm and b = 0.25 mm, adopted from Hu et al. [23]. The computational domain and boundary conditions are illustrated in Fig. 23. The computational domain has been carved out of the schematic shown in Fig. 22, where its location is shown in red dashed rectangle. To clearly show the liquid-gas interface and the sharp edges of the hole, the simulation setup is flipped upside down (note the gravity direction in Figs. 22 and 23), and the top solid surface is also removed, although its effects are incorporated in the computational domain using the appropriate boundary conditions. Leveraging the symmetry of the problem, only one hole was considered in the simulation. Symmetry boundary conditions were used at the lateral boundaries as shown in Fig. 23. Water is injected into the computational domain from the left boundary at $u_{\rm in} = 0.025$ m/s with the aid of an inlet velocity boundary condition. An outlet boundary condition at the opposite side allows the fluid out of the domain. An advancing contact angle of B° 0 was used at both the top and bottom surfaces. Taking the characteristic length B° 1 mm and characteristic velocity B° 2 was used at both the non-dimensional numbers characterizing this problem are B° 3 and B° 4 and B° 5 and 16 cells-per-height (CPH).

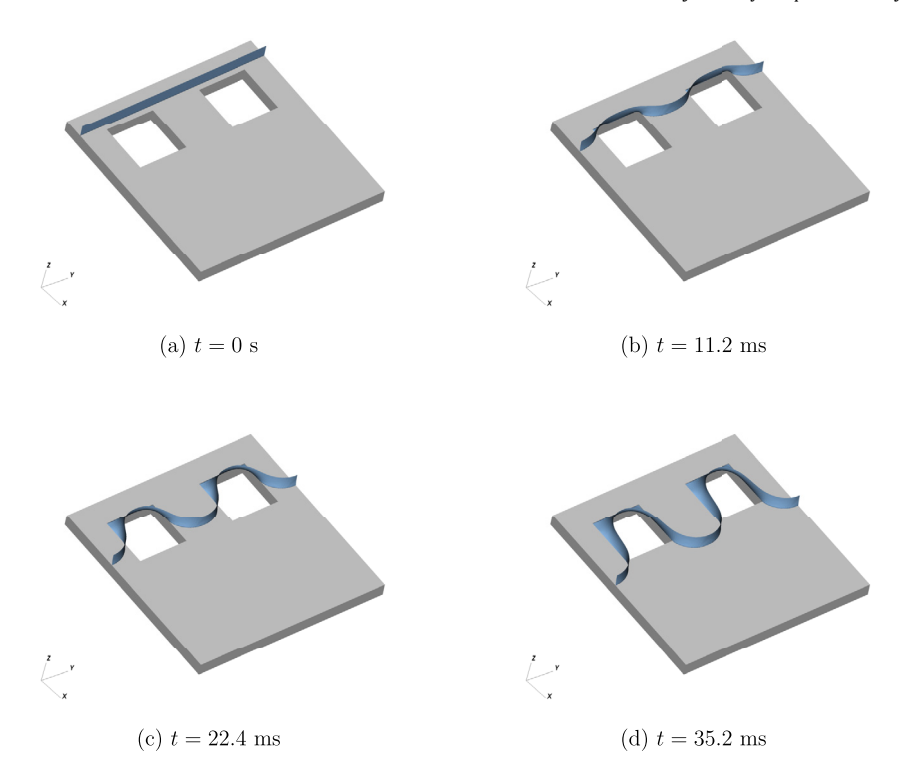


Fig. 24. Simulation results showing the water-air interface (blue) traveling past a row of square holes in a parallel gap and discontinuous pinning of the contact line at the bottom surface along the square hole edges. The top solid surface is not shown but the contact line formed on it is visible. We = 0.35 and Ca = 0.026

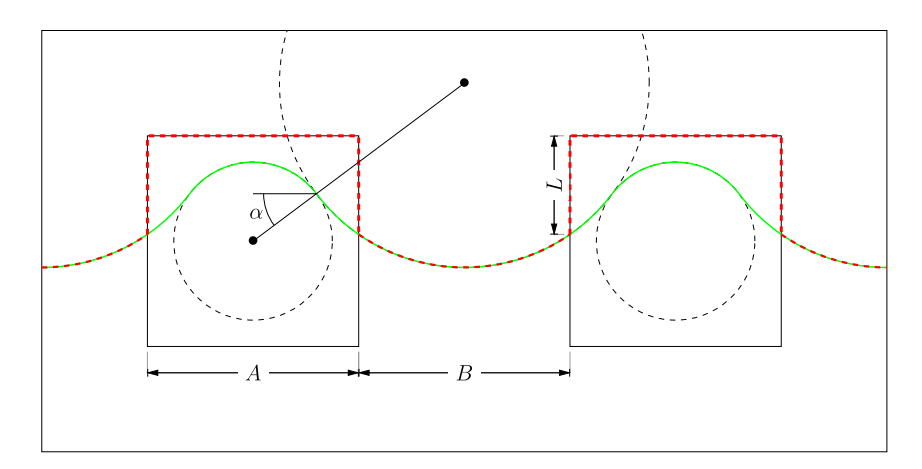


Fig. 25. Length L and angle α used for comparison between our results and the work by Hu et al. [23]. The contact line pinned at the solid surface containing the square holes is shown in red. The contact line on the opposite smooth surface is shown in green.

Fig. 24 presents the results from the 16 CPH simulation, showing the evolution and pinning of the water-air interface (blue) as it travels past the row of holes. Note that using the symmetry of the problem, the computational domain is mirrored once to include two holes in the figures. The top solid surface, obtained after flipping the setup in Fig. 22 upside down, is not shown for visibility of the water-air interface. Contact lines exist on both the top and bottom solid surfaces, but only the contact line on the bottom solid surface, which includes the holes, will undergo pinning. The results clearly show that a portion of the water-air interface is arrested at the hole edges due to discontinuous pinning, while the remaining part of the interface continues to travel in the space between the holes.

Next, we quantitatively compare the computational results with Hu et al. [23], who studied this problem both experimentally and analytically at the same A, B and h. The quantities used for the comparison include: angles θ_1 and α and length L, shown in Figs. 22 and 25. Angle θ_1 is between the liquid-gas interface and the edge of the holes on the corresponding surface, as illustrated in Fig. 22. Angle α is formed by the lateral line and the line joining the centers of two circles

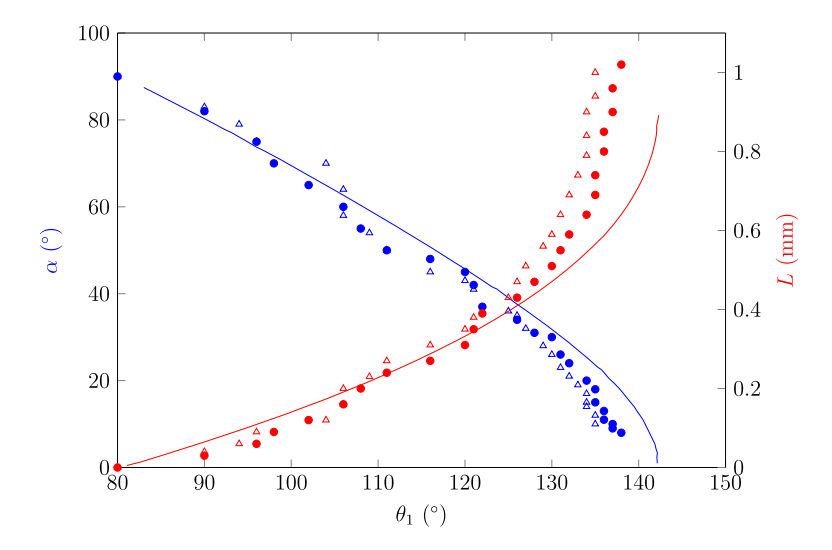


Fig. 26. Variation of shape parameters α (blue; left axis) and L (red; right axis) against θ_1 . The results from the simulations at two grid resolutions of 8 (\triangle symbol) and 16 CPH (\bullet symbol) are compared against the theoretical model (solid line) of Hu et al. [23].

containing the contact lines formed on the bottom and top surfaces as shown in Fig. 25. The contact line shown in red is pinned by the holes, while that shown in green is in contact with the opposite smooth surface. The same figure also shows the length L, which is the distance between the trailing lateral edge of the hole and the point where the contact line separates from the side edge of the hole. The above quantities are evaluated at 8 and 16 CPH simulations. In the present work, the quantities α , L and θ_1 were measured from the isosurface visualized in the Visit software [9] during post-processing. For computing α the inflection point on the isosurface is first identified, followed by measurement of normal orientation at that point. The theoretical expressions for $\alpha(\theta_1)$ and $L(\theta_1)$, which were rigorously derived by Hu et al. [23] are summarized here:

$$\alpha = \arccos\left(\frac{\Delta p \left(B + 2L_0\right)}{2\sigma}\right) \tag{22}$$

where,

$$\Delta p = \frac{(A+B) - (S/h)}{A+B} \frac{\sigma}{h} (\cos \theta_a - \cos \theta_1)$$
 (23)

$$L_0 = h \tan\left(\frac{\theta_1 - \theta_a}{2}\right) \tag{24}$$

$$S = Bh + 2r_2^2 \left(\sin \theta_1 \cos \theta_a + \frac{1}{2} \sin \theta_1 \cos \theta_1 - \frac{1}{2} \sin \theta_a \cos \theta_a + \frac{\theta_1 + \theta_a - \pi}{2} \right)$$
 (25)

$$r_2 = \frac{h}{\cos \theta_a + \cos \theta_1} \tag{26}$$

Also,

$$L = L_0 + L_1 + L_2 \tag{27}$$

where,

$$L_1 = r_4 \left(1 - \sin \alpha \right) \tag{28}$$

$$L_2 = \sqrt{r_3^2 - \left(\frac{B}{2}\right)} - r_3 \sin \alpha \tag{29}$$

$$r_3 = \frac{B + 2L_0}{2\cos\alpha} \tag{30}$$

$$r_4 = \frac{A - 2L_0}{2\cos\alpha} \tag{31}$$

Fig. 26 shows the variation of α and L against θ_1 as the interface moves past the row of holes and becomes pinned, along with the predictions from the theoretical model of Hu et al. [23]. The agreement between the theoretical model

and the simulation results is good when θ_1 is between 80° and 125°. As θ_1 goes beyond 125°, there is a discrepancy between the simulation results and the theoretical model, although the simulation results remain close to each other. The discrepancy can be attributed to the inertial effects that are neglected in the theoretical model but present and captured in the simulations. The theoretical model is based on a force balance on a stationary liquid-gas interface. In the simulations, however, the interface is continuously moving, and sufficient time may not be available for a redistribution of liquid mass to attain a state of minimum surface energy that is the basis of the theoretical model. The discrepancy between the theoretical and simulated results that occurs at high angles $\theta_1 > 125^{\circ}$ can be further explained by considering the small and large θ_1 regimes separately. The inlet flow in the simulations is equivalent to assuming increasing pressure at the liquid side. At small values of θ_1 , the interface deformation takes place both in the horizontal and vertical planes to balance this increase in pressure. At the pinned portion of the contact line, the interface stretches in the vertical plane to increase θ_1 and at the unpinned portion, the interface becomes more concave in the horizontal plane to reduce α . At large values of θ_1 , the interface stretching at the pinned portion does not contribute as much towards balancing the increased pressure on the liquid side as done by the increased concavity of the unpinned portion of contact line. This is evident from both theoretical and simulated results as demonstrated in Fig. 26. Here, the rate of decrease in α becomes higher at higher θ_1 . This difference in interface deformation between the pinned and unpinned portions of contact line at higher θ_1 becomes more exaggerated when there is flow. The flowing liquid prefers a path of the least resistance, i.e., flowing towards the unpinned portion of the contact line. Therefore, a higher rate of increase in L and a higher rate of decrease in α are present in the simulated results compared to the theoretical ones as can be seen in Fig. 26.

5. Summary and conclusions

This work presents a numerical scheme for modeling discontinuous contact line pinning in 3D and in the context of the Volume-of-Fluid method. The proposed scheme is focused on pinning at sharp straight edges, where the 3D Cartesian mesh conforms to the edge line. The discontinuous pinning is determined by solving a root-finding problem to adjust the orientation of PLIC polygons intersecting the edge line. Each polygon changes orientation by undergoing rotations, the axis of which is either normal or parallel to the edge line, and according to the stage of pinning, determined with the help of a geometrical toolbox. The proposed scheme was tested in discontinuous pinning of a sessile drop moving over a sharp edge, and water filling a parallel gap with a row of holes arresting the water contact line. In the latter, quantitative comparison with an experimental/theoretical study shows good agreement with the simulation results. Quantitative comparisons of the simulation results with and without the proposed numerical treatment of contact line pinning show a drastic difference. Future work includes extending the proposed scheme to model pinning at arbitrary shaped sharp edges that are non-conforming to the mesh.

CRediT authorship contribution statement

Ashish Pathak: Conceptualization, Writing – original draft. **Wen Jin:** Formal analysis, Investigation, Methodology, Software, Validation, Visualization. **Mehdi Raessi:** Funding acquisition, Supervision, Writing – review & editing.

Declaration of competing interest

The authors declare that they have no known competing financial interests or personal relationships that could have appeared to influence the work reported in this paper.

Data availability

Data will be made available on request.

Acknowledgements

The research support from the National Science Foundation under the CBET Grant Nos. 1336232 and 1904204 is gratefully acknowledged. MR acknowledges support from the UMass Dartmouth Marine and Undersea Technology Research Program (MUST) funded by the ONR award N00014-20-1-2849. The computations were performed on the HPC cluster of the UMass-Dartmouth's Center for Scientific Computing and Data Science Research supported by the ONR DURIP grant N00014-18-1-2255 "A Heterogeneous Terascale Computing Cluster for the Development and Efficient Implementation of High-Order Numerical Methods".

References

- [1] S. Afkhami, S. Zaleski, M. Bussmann, A mesh-dependent model for applying dynamic contact angles to VOF simulations, J. Comput. Phys. (ISSN 0021-9991) 228 (15) (Aug. 2009) 5370–5389, https://doi.org/10.1016/j.jcp.2009.04.027.
- [2] M. Baggio, B. Weigand, Numerical simulation of a drop impact on a superhydrophobic surface with a wire, Phys. Fluids (ISSN 1070-6631) 31 (11) (Nov. 2019) 112107, https://doi.org/10.1063/1.5123593.

- [3] J. Berthier, V.-M. Tran, F. Mittler, N. Sarrut, The physics of a coflow micro-extractor: interface stability and optimal extraction length, Sens. Actuators A, Phys. (ISSN 0924-4247) 149 (1) (Jan. 2009) 56–64, https://doi.org/10.1016/j.sna.2008.10.005, https://linkinghub.elsevier.com/retrieve/pii/S0924424708005153.
- [4] J. Bico, C. Marzolin, D. Quéré, Pearl drops, Europhys. Lett. (ISSN 0295-5075) 47 (2) (July 1999) 220, https://doi.org/10.1209/epl/i1999-00548-y, https://iopscience.jop.org/article/10.1209/epl/i1999-00548-y/meta, Publisher: IOP Publishing.
- [5] J.U. Brackbill, D.B. Kothe, C. Zemach, A continuum method for modeling surface tension, J. Comput. Phys. (ISSN 0021-9991) 100 (2) (June 1992) 335-354, https://doi.org/10.1016/0021-9991(92)90240-Y.
- [6] M. Bussmann, A Three Dimensional Model of an Impacting Droplet, PhD thesis, University of Toronto, 2000.
- [7] M. Bussmann, J. Mostaghimi, S. Chandra, On a three-dimensional volume tracking model of droplet impact, Phys. Fluids 11 (6) (June 1999) 1406–1417, https://doi.org/10.1063/1.870005, ISSN 1070-6631, 1089-7666.
- [8] L. Cao, H.-H. Hu, D. Gao, Design and fabrication of micro-textures for inducing a superhydrophobic behavior on hydrophilic materials, Langmuir (ISSN 0743-7463) 23 (8) (Apr. 2007) 4310–4314, https://doi.org/10.1021/la063572r, Publisher: American Chemical Society.
- [9] H. Childs, E. Brugger, B. Whitlock, J. Meredith, S. Ahern, D. Pugmire, K. Biagas, M.C. Miller, C. Harrison, G.H. Weber, H. Krishnan, T. Fogal, A. Sanderson, C. Garth, E.W. Bethel, D. Camp, O. Rubel, M. Durant, J.M. Favre, P. Navratil, Visit: An End-User Tool for Visualizing and Analyzing Very Large Data, October 2012, https://visit.llnl.gov.
- [10] A.J. Chorin, Numerical solution of the Navier-Stokes equations, Math. Comput. 22 (104) (1968) 745–762, https://doi.org/10.1090/S0025-5718-1968-0242392-2, ISSN 1088-6842, 0025-5718.
- [11] H. Ding, P.D.M. Spelt, Onset of motion of a three-dimensional droplet on a wall in shear flow at moderate Reynolds numbers, J. Fluid Mech. 599 (Mar. 2008) 341–362, https://doi.org/10.1017/S0022112008000190, ISSN 0022-1120, 1469-7645.
- [12] J.-B. Dupont, D. Legendre, Numerical simulation of static and sliding drop with contact angle hysteresis, J. Comput. Phys. (ISSN 0021-9991) 229 (7) (Apr. 2010) 2453-2478, https://doi.org/10.1016/j.jcp.2009.07.034.
- [13] F. Fahrni, A. Zimmermann, Coating Device, Google Patents, Aug. 1978.
- [14] G. Fang, A. Amirfazli, Understanding the edge effect in wetting: a thermodynamic approach, Langmuir (ISSN 0743-7463) 28 (25) (June 2012) 9421–9430, https://doi.org/10.1021/la301623h, Publisher: American Chemical Society.
- [15] P.A. Ferdowsi, Combined numerical and thermodynamic analysis of drop imbibition into an axisymmetric open capillary, Thesis, University of Toronto, Toronto, Canada, Aug. 2012, https://tspace.library.utoronto.ca/handle/1807/32709, Accepted: 2012-08-21T17:55:43Z.
- [16] P.A. Ferdowsi, M. Bussmann, Numerical treatment of contact line motion near a sharp corner, in: The European Community on Computational Methods in Applied Sciences, Lisbon, Portugal, June 2010, p. 13.
- [17] M.M. Francois, S.J. Cummins, E.D. Dendy, D.B. Kothe, J.M. Sicilian, M.W. Williams, A balanced-force algorithm for continuous and sharp interfacial surface tension models within a volume tracking framework, J. Comput. Phys. (ISSN 0021-9991) 213 (1) (Mar. 2006) 141–173, https://doi.org/10.1016/j.jcp.2005.08.004.
- [18] J.W. Gibbs, Scientific Papers of J. Willard Gibbs, in Two Volumes, vol. 1, Longmansm, Green, 1906.
- [19] F. Goldschmidtboeing, M. Rabold, P. Woias, Strategies for void-free liquid filling of micro cavities, J. Micromech. Microeng. (ISSN 0960-1317) 16 (7) (May 2006) 1321–1330, https://doi.org/10.1088/0960-1317/16/7/029, Publisher: IOP Publishing.
- [20] W.D. Harkins, F.E. Brown, The determination of surface tension (free surface energy), and the weight of falling drops: the surface tension of water and benzene by the capillary height method. I. Am. Chem. Soc. 41 (4) (1919) 499–524. Publisher: ACS Publications.
- [21] F.H. Harlow, J.E. Welch, Numerical calculation of time-dependent viscous incompressible flow of fluid with free surface, Phys. Fluids (ISSN 0031-9171) 8 (12) (Dec. 1965) 2182–2189, https://doi.org/10.1063/1.1761178.
- [22] B. He, N.A. Patankar, J. Lee, Multiple equilibrium droplet shapes and design criterion for rough hydrophobic surfaces, Langmuir 19 (12) (June 2003) 4999–5003, https://doi.org/10.1021/la0268348, https://pubs.acs.org/doi/10.1021/la0268348, ISSN 0743-7463, 1520-5827.
- [23] L. Hu, M. Wu, W. Chen, H. Xie, X. Fu, Discontinuous pinning effect by a hole row to the gas-liquid interface in a parallel gap, Exp. Therm. Fluid Sci. (ISSN 0894-1777) 87 (Oct. 2017) 50-59, https://doi.org/10.1016/j.expthermflusci.2017.04.022, https://linkinghub.elsevier.com/retrieve/pii/S0894177717301255.
- [24] M. Im, H. Im, J.-H. Lee, J.-B. Yoon, Y.-K. Choi, A robust superhydrophobic and superoleophobic surface with inverse-trapezoidal microstructures on a large transparent flexible substrate, Soft Matter (ISSN 1744-6848) 6 (7) (Mar. 2010) 1401–1404, https://doi.org/10.1039/B925970H, https://pubs.rsc.org/en/content/articlelanding/2010/sm/b925970h, Publisher: The Royal Society of Chemistry.
- [25] C. Jiang, X. Li, H. Tian, C. Wang, J. Shao, Y. Ding, L. Wang, Lateral flow through a parallel gap driven by surface hydrophilicity and liquid edge pinning for creating microlens array, ACS Appl. Mater. Interfaces (ISSN 1944-8244) 6 (21) (Nov. 2014) 18450–18456, https://doi.org/10.1021/am506067v, Publisher: American Chemical Society.
- [26] K. Koch, B. Bhushan, Y. Chae Jung, W. Barthlott, Fabrication of artificial Lotus leaves and significance of hierarchical structure for superhydrophobicity and low adhesion, Soft Matter 5 (7) (2009) 1386–1393, https://doi.org/10.1039/B818940D, https://pubs.rsc.org/en/content/articlelanding/2009/sm/b818940d, Publisher: Royal Society of Chemistry.
- [27] H. Kusumaatmaja, C.M. Pooley, S. Girardo, D. Pisignano, J.M. Yeomans, Capillary filling in patterned channels, Phys. Rev. 77 (6) (June 2008) 067301, https://doi.org/10.1103/PhysRevE.77.067301, Publisher: American Physical Society.
- [28] X. Lv, Q. Zou, Y. Zhao, D. Reeve, A novel coupled level set and volume of fluid method for sharp interface capturing on 3D tetrahedral grids, J. Comput. Phys. (ISSN 0021-9991) 229 (7) (Apr. 2010) 2573–2604, https://doi.org/10.1016/j.jcp.2009.12.005.
- [29] G.W. Maier, O.D. Brown, Die Coating Apparatus with Surface Covering, Google Patents, June 1998.
- [30] J.F. Oliver, C. Huh, S.G. Mason, Resistance to spreading of liquids by sharp edges, J. Colloid Interface Sci. (ISSN 0021-9797) 59 (3) (May 1977) 568-581, https://doi.org/10.1016/0021-9797(77)90052-2, https://www.sciencedirect.com/science/article/pii/0021979777900522.
- [31] A. Pathak, M. Raessi, A 3D, fully Eulerian, VOF-based solver to study the interaction between two fluids and moving rigid bodies using the fictitious domain method, J. Comput. Phys. (ISSN 0021-9991) 311 (Apr. 2016) 87–113, https://doi.org/10.1016/j.jcp.2016.01.025.
- [32] A. Pathak, M. Raessi, A three-dimensional Volume-of-Fluid method for reconstructing and advecting three-material interfaces forming contact lines, J. Comput. Phys. (ISSN 0021-9991) 307 (Feb. 2016) 550–573, https://doi.org/10.1016/j.jcp.2015.11.062.
- [33] A. Pathak, C. Freniere, M. Raessi, Advanced computational simulations of water waves interacting with wave energy converters, Eur. J. Comput. Mech. (ISSN 1779-7179) 26 (1–2) (Mar. 2017) 172–204, https://doi.org/10.1080/17797179.2017.1306829.
- [34] C.S. Peskin, Numerical analysis of blood flow in the heart, J. Comput. Phys. (ISSN 0021-9991) 25 (3) (Nov. 1977) 220-252, https://doi.org/10.1016/0021-9991(77)90100-0.
- [35] W.H. Press, S.A. Teukolsky, W.T. Vetterling, B.P. Flannery, Numerical Recipes in C: The Art of Scientific Computing, second edition, Cambridge University Press, New York, NY, USA, ISBN 0-521-43108-5, 1992.
- [36] S. Reddy, R.T. Bonnecaze, Simulation of fluid flow in the step and flash imprint lithography process, Microelectron. Eng. (ISSN 0167-9317) 82 (1) (Sept. 2005) 60–70, https://doi.org/10.1016/j.mee.2005.06.002, https://www.sciencedirect.com/science/article/pii/S0167931705003060.
- [37] O.J. Romero, L.E. Scriven, M. d, S. Carvalho, Effect of curvature of coating die edges on the pinning of contact line, AIChE J. (ISSN 1547-5905) 52 (2) (2006) 447-455, https://doi.org/10.1002/aic.10672, https://aiche.onlinelibrary.wiley.com/doi/pdf/10.1002/aic.10672.
- [38] M. Rudman, A volume-tracking method for incompressible multifluid flows with large density variations, Int. J. Numer. Methods Fluids (ISSN 1097-0363) 28 (2) (1998) 357-378, https://doi.org/10.1002/(SICI)1097-0363(19980815)28:2<357::AID-FLD750>3.0.CO;2-D.

- [39] S. Shin, J. Chergui, D. Juric, Direct simulation of multiphase flows with modeling of dynamic interface contact angle, Theor. Comput. Fluid Dyn. 32 (5) (Oct. 2018) 655–687, https://doi.org/10.1007/s00162-018-0470-4, ISSN 0935-4964, 1432-2250.
- [40] P.D.M. Spelt, A level-set approach for simulations of flows with multiple moving contact lines with hysteresis, J. Comput. Phys. (ISSN 0021-9991) 207 (2) (Aug. 2005) 389–404, https://doi.org/10.1016/j.jcp.2005.01.016.
- [41] L. Wang, H.-b. Huang, X.-Y. Lu, Scheme for contact angle and its hysteresis in a multiphase lattice Boltzmann method, Phys. Rev. E 87 (1) (Jan. 2013) 013301, https://doi.org/10.1103/PhysRevE.87.013301, ISSN 1539-3755, 1550-2376.
- [42] M.C. Wilkinson, Extended use of, and comments on, the drop-weight (drop-volume) technique for the determination of surface and interfacial tensions, J. Colloid Interface Sci. 40 (1) (1972) 14–26, Publisher: Elsevier.
- [43] H. Wu, K. Zhu, B. Wu, J. Lou, Z. Zhang, G. Chai, Influence of structured sidewalls on the wetting states and superhydrophobic stability of surfaces with dual-scale roughness, Appl. Surf. Sci. (ISSN 0169-4332) 382 (Sept. 2016) 111–120, https://doi.org/10.1016/j.apsusc.2016.04.101, https://www.sciencedirect.com/science/article/pii/S0169433216308534.
- [44] D.L. Youngs, An interface tracking method for a 3D Eulerian hydrodynamics code, Technical Report 44/92/35, AWRE Design Mathematics Division, 1984.
- [45] P. Yue, Thermodynamically consistent phase-field modelling of contact angle hysteresis, J. Fluid Mech. 899 (Sept. 2020) A15, https://doi.org/10.1017/jfm.2020.465, ISSN 0022-1120, 1469-7645.
- [46] J. Zhang, P. Yue, A level-set method for moving contact lines with contact angle hysteresis, J. Comput. Phys. (ISSN 0021-9991) 418 (Oct. 2020) 109636, https://doi.org/10.1016/j.jcp.2020.109636.
- [47] H. Zhao, K.-C. Park, K.-Y. Law, Effect of surface texturing on superoleophobicity, contact angle hysteresis, and "robustness", Langmuir (ISSN 0743-7463) 28 (42) (Oct. 2012) 14925–14934, https://doi.org/10.1021/la302765t, Publisher: American Chemical Society.